This paper has been published in IEEE TRANSACTIONS ON INSTRUMENTATION AND MEASUREMENT UNDER DOI 10.1109/TIM.2022.3200107

Artifact Mitigation for High-Resolution Near-Field SAR Images by Means of Conditional Generative Adversarial Networks

Jaime Laviada, Guillermo Álvarez-Narciandi, and Fernando Las-Heras, *Senior Member, IEEE*

***Abstract*— This work presents an approach to enhance the quality of high-resolution images obtained by means of systems relying on synthetic aperture radar (SAR). For this purpose, a deep learning method called conditional generative adversarial networks (cGAN) is applied to the imager outcome when it is prone to suffer artifacts. This is specially the case of novel systems pushing the limits of SAR (e.g., irregular sampling, multilayered media, etc.) resulting in very chaotic clutter and image artifacts that cannot be easily removed with conventional approaches. The cGAN can be trained to detect high-level characteristic features in the image (e.g., parts of a scissor blade) so another output based on these detected features can be tailored. In other words, it can translate features contaminated by artifacts into clean features, effectively improving the quality of SAR images. Unlike other deep learning approaches, the training of the involved neural networks tends to be stable thanks to the structure based on two competing subsystems. The proposed approach is illustrated using simulated and measurement data in the context of two advanced near-field SAR systems considering: i) cylindrical multilayered media, and ii) freehand acquisitions. Results show that cGANs clearly outperform conventional approaches removing most of the artifacts, enabling to produce a clean output image.**

***Index Terms*—mmWave imaging, synthetic aperture radar, stratified media imaging, freehand, deep learning, generative adversarial net, clutter.**

I. Introduction

SYNTHETIC aperture radar (SAR) is able to generate electromagnetic images enabling the capability to 'see' through some visually opaque elements (clouds, fog, paper, etc.). This technique became firstly popular in the remote sensing field in order to obtain aerial images [1]. However, in the recent years, SAR has also become a very powerful technique at closer ranges, which are typically in the near-field of the synthetic aperture, and using higher frequencies to generate high-resolution images. Thanks to its characteristics, SAR has become the cornerstone of instrumentation for people screening [2], [3], nondestructive evaluation [4], [5] or medical imaging [6].

This work was supported in part by the Ministerio de Ciencia, Innovación y Universidades of Spain/Fondo Europeo de Desarrollo Regional (FEDER) under Project PID2021-122697OB-I00, by Principado de Asturias under project AYUD/2021/51706 and by the Spanish Ministry of Universities and European Union (NextGenerationEU Fund) under Project MU-21-UP2021-030.

Jaime Laviada and Fernando Las-Heras are with the Department of Electrical Engineering, University of Oviedo, Gijón, 33203, Spain (e-mail: laviadajaime@uniovi.es; flasheras@uniovi.es). Guillermo Álvarez Narciandi is with the Department of Electrical Engineering, University of Oviedo, Gijón and with the Centre for Wireless Innovation, Queen's University Belfast, Belfast, United Kingdom (alvareznguillermo@uniovi.es).

Synthetic aperture imaging has been traditionally applied under the hypotheses of free-space propagation and regular sampling in the space domain (e.g., [7], [8], [9]). However, last advances have shown that the SAR paradigm can be extended to deal with stratified media as well as nonregular sampling. In the first case, approaches to deal with planar- and cylindrical-mulilayered media have been recently demonstrated [10], [11], [12] enabling the detection of anomalies (flaws, voids, corrosion, etc.) for nondestructive evaluation. In the second case, UAV and freehand imaging have brought a new horizon of possibilities for detecting landmines with GPR [13] or turning cellphones into handheld scanners [14] at the expense of relying on nonregular sampling [15], [16].

This kind of approaches, though able to provide very insightful information, are pushing the limits of the imaging capabilities. This effort together with some of the limitations inherent to conventional synthetic aperture imaging result in systems which are prone to suffer from unwanted effects in terms of artifacts and clutter.

In order to mitigate the aforementioned effects, conventional deterministic techniques have been usually applied. The most straightforward approach is the use of a low pass filter, as artifacts are usually included by means of fast spatial variations in the image. Although this generic approach mitigates many of the artifacts, it is usually not enough to increase the contrast of the targets with respect to the background and, moreover, it reduces the resolution of the image.

Another technique to mitigate the artifacts is the use of singular value decomposition (SVD) in order to remove the contributions from some interfaces (e.g., ground-air in land-mine detection or wall in the context of through-the-wall-imaging) as they are one of the main contributors to unwanted effects [17], [13]. A similar approach has also been proposed using the principal component analysis to filter out artifacts [18].

The previous approaches can be applied to a broad number of problems, achieving a good performance. However, specific approaches, tailored for specific problems, are expected to provide a better performance. In the last years, deep learning has shown a great potential for image processing. For example, the use of *regional convolutional neural network* (R-CNN) has shown the ability to detect and classify clutter from radar images [19], [20], though it is usually limited to tag rectangular regions. Other deep learning approaches are the *conditional generative adversarial networks* (cGANs) [21], which have shown an excellent performance in translating images with

some (deep or abstract) features into new images showing other (or potentially similar) features.

In the last years, the usage of cGANs has been vast, including a large number of applications related to systems based on SAR. For example, cGANs have been used to generate aerial SAR images from optical images [22], [23], [24], [25] to generate realistic colored images from SAR images [26] or to detect targets from aerial images [27]. Although not based on synthetic aperture techniques, it is worthy to note that this deep learning approach has also been used to translate low resolution images acquired by a small mmWave radar into high resolution depth images [28]. This is performed by training the system to translate those radar images into high resolution images coming from a light detection and ranging (LiDAR) instrument.

Thus, cGANs exhibit a great potential to tailor the processing of SAR images so that cleaner images can be generated from those ones contaminated with artifacts caused by complex imaging scenarios (e.g., multilayered scenarios), the additional challenges from some novel advanced SAR systems (e.g., irregular sampling), and some of the inherent limitations of SAR processing. To the best authors knowledge, although some deep learning approaches have been applied to the classification of targets in conventional radar approaches [29], [30] and to reduce the sea clutter [31], their application to clean high-resolution images coming from modern inspection systems based on near-field SAR has not been studied. In this paper, cGANs are adapted to improve the quality of near-field SAR images prone to artifacts. In particular, their impact in the images obtained by two very demanding imaging systems (SAR applied to stratified media and freehand measurements) is investigated, showing that this tool can provide a significant boost to the quality of the results.

The remainder of this paper is structured as follows. Section II provides a short-summary of near-field SAR imaging in order to emphasize the approximations behind each step that yield some of the main artifacts in SAR images. Next section presents the concept of cGANs and how they can be used to reduce the amount of clutter in SAR images. After that, in Section IV results illustrating the performance of the proposed approach are presented. Specifically, the case of cylindrically-multilayered media, e.g., a pipe, as well as sparse problems, e.g., when performing freehand scanning with a radar-on-chip, are discussed. Finally, the conclusions and future research lines are drawn in Section V. In addition, the training data images and target models are released so the results can be reproduced [32].

II. Artifact sources in advanced near-field imaging

SAR techniques, when applied to close targets, can achieve excellent resolution though they are not free of artifacts. In this section, we will consider some advanced imaging techniques based on SAR in order to understand the reason for these undesired effects. For the sake of simplicity, we will consider a monostatic formulation, though the same ideas can be applied to multistatic measurements, i.e., multiple input multiple output (MIMO) systems. This section provides an insight on the sources of the undesired effects which appear in SAR images due to approximations in the formulation. In addition to those imperfections, which are referred to as artifacts, other undersired effects could rise due to the hardware implementation of the imagers, as it can differ from the ideal models of transmitters and receivers, increasing the unwanted artifacts (e.g., radiation pattern changes [33] or element deviation [34]).

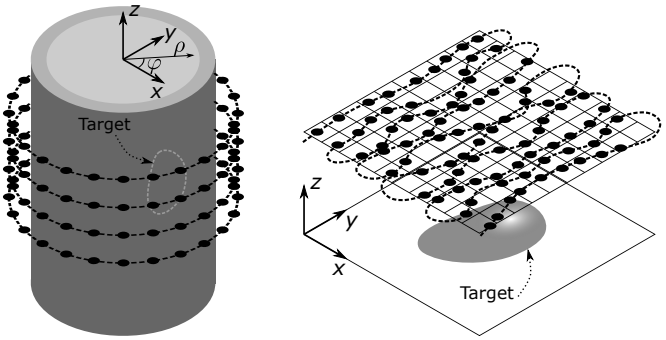

(a) (b)

Fig. 1. Different SAR approaches: (a) imaging of cylindrically-layered media; (b) planar freehand imaging. Black dots denote acquisition positions.

SAR imaging is based on acquiring the field scattered by the scene from a set of positions, which are usually equally-spaced on a canonical surface such as a cylinder or a plane (see Fig. 1). If the scene has a number of targets, described by a reflectivity function $\Gamma(\vec{r}')$, then it is usual to model the received field $S(\vec{r}, f)$ as:

$$S(\vec{r}, f) \approx \int_{r'} \Gamma(\vec{r}') G_{rt}\left(\vec{r}, \vec{r}', f\right) d\vec{r}', \tag{1}$$

wherein f is the acquisition frequency, $\vec{r}$ is the observation point where the transmitter/receiver is placed and $G_{rt}\left(\vec{r}, \vec{r}', f\right)$ is the roundtrip Green's function [10]. Synthetic aperture imaging pursues to retrieve an approximation of the reflectivity $\Gamma(\vec{r}')$, which represents the image.

It is important to note that (1) takes into account the reflections corresponding to the media modeled by the Green's function (e.g, multilayered problems). Nevertheless, it is important to note that (1) does *not* take into account multiple reflections between the targets. Consequently, multipath is only partially considered so it can yield some undesired artifacts. Moreover, this propagation model does not account for depolarization concerns, which can be also a source of artifacts.

In homogeneous media or under some special conditions based on the background medium and acquisition surface, (1) can be expressed as a convolution in terms of the surface coordinates, which will be denoted as u and v. Consequently, the reflectivity $\Gamma(\vec{r}')$ can be retrieved by means of a deconvolution. However, it is well-known that, in general, convolution cannot be perfectly inverted. Some possibilities are the use of Wiener deconvolution (e.g., [10]) or a matched filter [35]. The latter results in the following approximation:

$$\Gamma_f(u', v', w', f) \approx \mathcal{F}\left\{S(u, v, f)\tilde{G}^*_{rt}\left(k_u, k_v, w', f\right)\right\}, \tag{2}$$

wherein $\mathcal{F}\{\cdot\}$ denotes Fourier transform, $\tilde{G}^*_{rt}$ is the complex conjugate of the Fourier transform of the round trip Green's function evaluated at the spatial frequencies k_u and k_v, and w denotes the third spatial coordinate to designate a point in space. For example, if cylindrically-stratified media is considered, then $u = \varphi$, $v = z$ and $w = \rho$.

Eq. (2) again includes some approximations, as the deconvolution is not perfectly accomplished, resulting in an additional source of artifacts. It is interesting to remark that, under free-space conditions and considering a XY planar acquisition, this matched filter approach, after neglecting amplitude constants, yields the very well-known formulation [7], [2]:

$$\Gamma_f(x', y', z', f) = \int_{x,y} S(x, y, f) e^{j\frac{4\pi f}{c}\sqrt{(x-x')^2+(y-y')^2(z-z_0)^2}} dxdy, \quad (3)$$

being c the speed of light in free space and z_0 the z coordinate of the acquisition plane.

In practice, the measurements $S(\vec{r}, f)$ cannot be done for a continuum of points with infinite length, so this truncation also introduces some extra artifacts. Moreover, some techniques, such as freehand imaging [15], require some flexibility of the sampling criteria as they cannot acquire equally-spaced samples. Although freehand imaging pursues to keep a global balance of the sampling, undesired contributions cannot be completely filtered out.

Finally, it is interesting to note that, if multiple frequencies are available, the previous results can be coherently integrated to improve the quality of the image:

$$\Gamma(u', v', w') = \int_f \Gamma_f(u', v', w', f) df. \quad (4)$$

Thus, the approximations done in some SAR-based formulations yield to imperfect results.

III. SAR IMAGE TRANSLATION BY CGANS

Generative adversarial nets (GANs) are generative systems, which can produce an output according to a certain distribution learned by the system. A popular example is the synthesis of new face images [36]. In contrast to other approaches such as a pure neural network, GANs employ a training system consisting of two adversarial networks competing with each other in a *minmax* game. The first net is referred to as *generator (*G*)* and it generates an output according to a target distribution. The input of the generator is typically chosen from a latent space, which has a stochastic nature in many cases. The second net is known as *discriminator* (*D*) and it has a binary output that determines if the output of the generator follows the desired distribution or not. Both networks are usually implemented by means of convolutional neural networks (CNNs).

A special case of GANs are the conditional GANs. In this case, the output of the generator is conditioned by a particular input. Although their uses are multiple, one of the most successful is their application to *image to image translation* so that the input condition is the input image. Some examples are night to day picture or satellite to street view map translation [37] as well as precipitation maps generation from multispectral data [38], image deraining [39], restoring ancient handwriting [40], and replacing conventional deconvolution for astronomical image enhancement [41].

In order to describe the system, let us consider the different kind of images that will be involved throughout the remainder of this work (see Fig. 2):

- Real images: they will be referred to as I_{ref}. They consist of a representation of the scene to be reconstructed (i.e., the ideal output of the imaging system). They are only available during the training phase of the system as the scene is unknown during the conventional operation.
- SAR images with artifacts: they will be referred to as I_{in}. These images correspond to the output of conventional imaging systems if no further processing is applied. These images are used during the training as well as during the conventional operation. It should be noted that due to the high amount of required images for the training, it is usually needed to resort to synthesized images (e.g., from simulations), as the generation of a complete dataset from measurements may not be feasible. Nonetheless, as it will be shown in Section IV, a cGAN trained with synthetic data is also able to clean SAR images obtained from measurement data. Depending on the available data, the input image can have one or two channels. In general, the input image will consist of two channels with the real and imaginary part of the reflectivity. However, it is usual that the phase information of this image is not available as it requires a reliable calibration. In those cases, a single channel is used as input.
- Corrected images: they are generated by the cGAN from I_{in} and correspond to the output of the aforementioned generator G and, therefore, they are denoted by $G(I_{in})$. Thus, they try to provide a result similar to the real scene. They are used during the training as well as during the normal operation.

Once the involved images have been detailed, let us focused on the different CNNs comprising the system. First, the *discriminator* will be described. This CNN is only used during the training stage and it should be able to determine if an image has been (artificially) generated from a given input or not. Thus, the input of the discriminator are two images. On the one hand, the image with artifacts, I_{in}. On the other hand, a second image which will be classified by the discrimator as artificial or real. According to the goal of the discriminator, if this second argument is a real image I_{ref} , then the output should be $D\left(I_{\text{in}}, I_{\text{ref}}\right) = 1$. On the other hand, if the second argument is a generated (i.e., fake) image $G\left(I_{\text{in}}\right)$, then $D\left(I_{\text{in}}, G\left(I_{\text{in}}\right)\right) = 0$. Consequently, the discriminator can be trained according to the following loss function [36] so that it provides images as close as possible to real scenes:

$$\mathcal{L}\{G\} = \max_D \left(E_{I_{\text{ref}}}\left[\log D\left(I_{\text{in}}, I_{\text{ref}}\right)\right] + E_{I_{\text{in}}}\left[\log\left(1 - D\left(I_{\text{in}}, G\left(I_{\text{in}}\right)\right)\right)\right]\right), \quad (5)$$

where E denotes mathematical expectation.

The second CNN involved in the cGAN is the *generator*, whose goal, as previously introduced, is to fool the discrim-

inator. A proper training of the generator should pursue the minimization of the previous loss function and, therefore, the cGAN optimization follows the *minmax* problem described by:

$$\min_{G}\left(\max_{D}\left(E_{I_{\text{ref}}}\left[\log D\left(I_{\text{in}},I_{\text{ref}}\right)\right]+ \right.\right. \\ \left.\left.+E_{I_{\text{in}}}\left[\log\left(1-D\left(I_{\text{in}},G\left(I_{\text{in}}\right)\right)\right)\right]\right)\right). \quad (6)$$

In contrast to other conventional CNN training, typically based on minimizing some kind of distance, this *minmax* game involves a discriminator evolving during the training and, therefore, it forces the generator to also improve. In general, it has been observed that this approach results in more natural images.

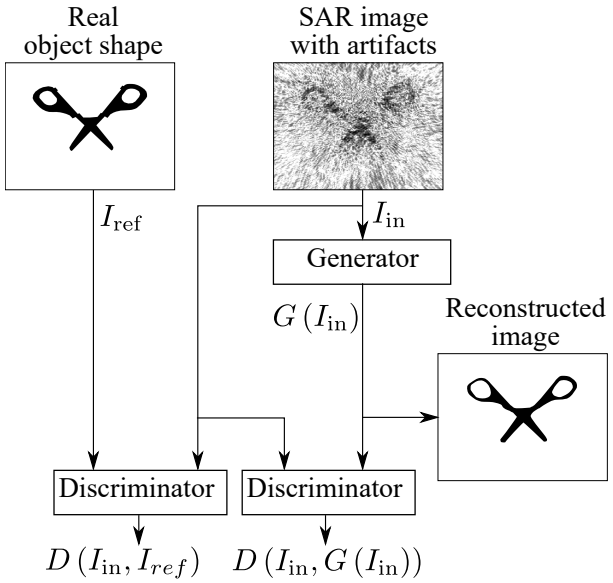

Fig. 2. Overall view of the training of a cGAN for cleaning artifacts in near-field SAR images. After training, only the generator net is used.

In order to train the system, pairs of images comprising the real targets and their corresponding SAR image must be used. After that, the generator and discriminator are optimized according to (6). Once the training is finished, the discriminator is not used anymore. Instead, the imperfect images are used as input to the generator, which is expected to generate images resembling real scenes (i.e., cleaned SAR images) so a trained discriminator cannot tell if they are synthetic or not.

The architecture of the two networks is selected according to pix2pix [37] and, in particular, the Matlab port [42]. This architecture is depicted in Fig. 3. The overall idea of the generator architecture is to move information from a pixel encoding to a feature encoding, which is completely approached at the intermediate stages. After that, the inverse process is performed so from some generic features, specific features are built until creating a conventional pixel image (without artifacts). The first layers of the down blocks are expected to detect low-level features (e.g., edges) whereas deeper layers, fed by the previous features, can detect more complex shapes like the handles of the scissors, though more abstract shapes are usually tailored. In the first down block, the batch normalization layer is not included as the input images are already normalized. On the other hand, the up blocks perform transposed convolutions (i.e., conventional convolutions with a modified feature input) in order to upscale the image until generating the final output image $G\left(I_{\text{in}}\right)$. Skip connections are also enabled between the down and up blocks so that input feature information is also directly available during the upscaling stage. This output image is expected to be a clean image of the target, though not a pixel by pixel copy of the original one as small features of the original target will be lost.

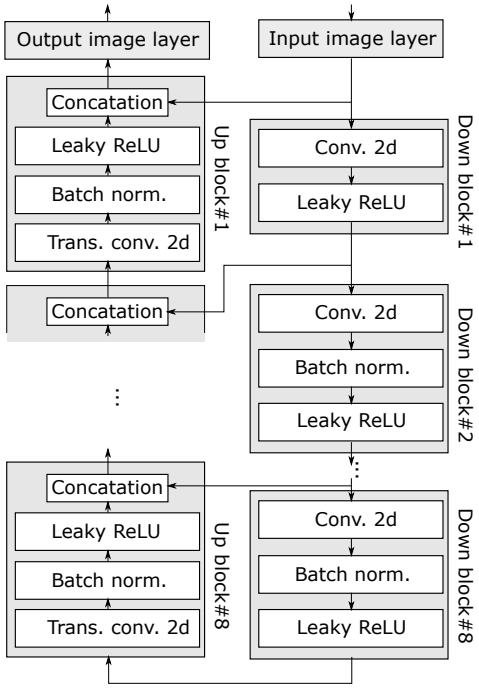

Fig. 3. Generator architecture.

The discriminator has the same layer architecture of the generator down blocks with two main differences. The input layer has a number of channels corresponding to the total number of channels (i.e., input plus output channels) so both images feed the discriminator. In addition, the output layer, which is located after the last up block, consists of a convolutional layer with a single filter of size 1×1 in order to classify the generated image as either real or fake.

IV. Results

In order to validate the capabilities of cGANs, two different SAR problems prone to artifacts are considered. The first one involves a cylindrically-layered media, which is prone to undesired effects due to the complexity of the underlying deconvolution. The second example consists of a freehand SAR approach, in which the source of artifacts is mainly the sparse and non-uniform data acquisition. In the first case, synthetic data is used to assess the capacity of the cGAN to exploit reliable amplitude and phase information whereas the second case only uses the amplitude of the reflectivity image obtained from measurements.

The cGAN implementation used in this work is based on the pix2pix port available for Matlab [42]. Unless otherwise stated,

the parameters used for the cGANs are the ones summarized in Table I. In addition, the training set images are flipped horizontally and vertically to increase the available dataset.

The number of filters at each layer follows the original pix2pix sizes [37]. Thus, the number of layers of the generator is set to 8 with the default size 64, 128, 256, 512, 512, 512, 512 and 512. In a similar fashion, the discriminator consists of 4 down blocks using also the default sizes: 64, 128, 256 and 512.

Unless otherwise stated, the reported CPU times have been measured in a laptop equipped with a CPU Intel Core I7 at 2.6GHz, 32GB of RAM and a GPU Nvidia Geforce RTX 2060. In order to execute the code, Matlab 2020a has been used.

Regarding the processing time, it is important to remark that the cGANs, as most of machine learning approaches, involve two different stages: training and production. Training time depends on the architecture of the networks as well as the number of training pairs. In addition, if it is necessary to resort to synthetic data for the training, the time required to generate this data can also be significant (depending on the solver and number of simulations). Although the training can be time consuming, it only needs to be done once so the most insightful time regarding the use of the cGAN is the evaluation time once they are in production (i.e., the time required by the cGAN to produce an output based on an input image), which will be described for the different examples.

Table I
cGANs PARAMETERS.

Input/output size	Leaky ReLU scale	Filter size	Stride
256×256	0.2	4×4	2×2

In order to quantify the error, the L_1-norm between the real images and the images cleaned by the cGAN will be shown. This norm is defined as:

$$L_1\{I, I_{ref}\} = \langle |I - I_{ref}| \rangle$$

wherein $\langle \cdot \rangle$ denotes the mean value along all the dimensions and channels of the image.

A. SAR for cylindrically-layered media

SAR for cylindrically-layered media, depicted in Fig. 1a, is a challenging problem because the SAR techniques, though able to focus the reflectivity energy around the targets, are prone to artifacts around them, complicating their detection.

In this example, a pipe-like geometry with three different layers surrounded by air is simulated to analyze the performance of cGAN. The radii of the different layers are 12, 10 and 5 cm and the corresponding relative permittivity constants are 2, 3 and 1 in order to simulate a hollow pipe.

The pipe is scanned with a monostatic setup measuring at a distance of 25 cm from the center. The number of equally-spaced angles is set to 420. In this setup, only XY slices are considered and, therefore, the samples are acquired at a single z plane. The scanning frequencies are set to 51 covering the X band (8.2 GHz-12.4 GHz).

In this example, the targets are considered to be electrically small so they can be modeled as point-like targets. Therefore the field simulated at each position (ρ, ϕ) is given by:

$$S(\rho, \phi, f) = \sum_{n=1}^{N} G_z\left(\rho, \rho_n', \phi - \phi_n', f\right), \tag{7}$$

wherein $G_z\left(\rho, \rho_n', \phi - \phi_n', f\right)$ denotes the z-component of the Green's function for a target at a position (ρ_n', ϕ_n') and an observation point (ρ, ϕ), and N is the total number of targets. The targets are supposed to be at the same z plane as the scanning plane. In order to compute the SAR images for this stratified problem, equations (2) and (4) are used.

In order to train the cGAN, images for several random targets are used. In particular, three blocks of 80 simulations are used consisting of problems with 1, 2 and 3 point-like targets, respectively. Consequently, the dataset consists of 240 images, which was augmented to 960 by flipping around the horizontal and vertical axes. SAR images are generated using (2) and (4), resulting in a two channel image encoding the real and imaginary parts of the reflectivity.

Regarding the output image, since the layer radii are supposed to be known, only the target positions are the real unknowns. Consequently, a single channel output image would be enough. Nevertheless, in order to include a more complex setup, a three channel output image is considered. Thus, it is also possible to use colors to label the different areas of the output image. In particular, the background media color is set to white, whereas the targets are shown in black with a radius of 5 mm. Finally, the pipe layers are colored in red, green and blue from the outer to the inner layer, respectively.

The L_1-norm for the training images along the different iterations of the training is shown in Fig. 4 revealing that the training yields stable results, with a fast convergence rate.

Fig. 5 depicts some intermediate results for different pairs of the training set. The results are in agreement with the overall results of the L_1-norm pipe so, after 481 iterations, although the results are relevant, they are still blurred. A significant improvement is found after additional iterations.

After analyzing the training of the cGAN, several test results are shown in Fig. 6a for arbitrary target positions. SAR images show that the imaging technique is able to detect most of the targets but their position is not always clear with images populated by artifacts. Moreover, these artifacts are very dependent on the ρ coordinate.

Starting from the top, the first SAR image provides a fair resolution enabling an easy detection of the targets even for the human eye. In the next two cases (i.e., second and third rows), the target close to the center has a low contribution in the SAR image, which is dominated by the other two targets. Nevertheless, the cGAN is able to detect all of them correctly in both cases. In the fourth case, two very close targets are considered as well as an additional target. Although the SAR imaging technique is able to identify a high reflectivity level, it is clear that the SAR image is not enough to identify if there is more than one target. In this case, the cGAN is able

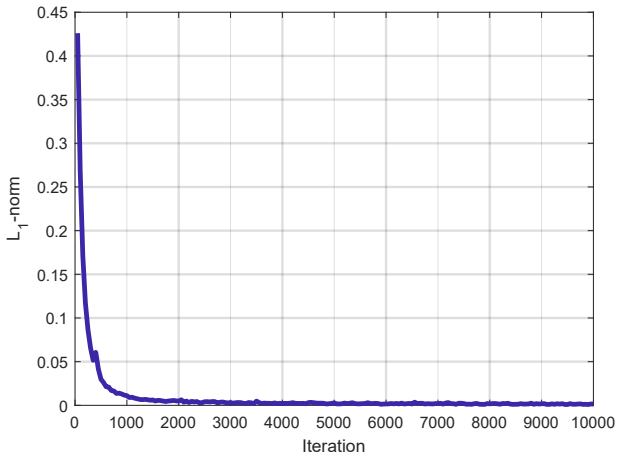

Fig. 4. L_1-norm for the training set for the cylindrically-layered media example.

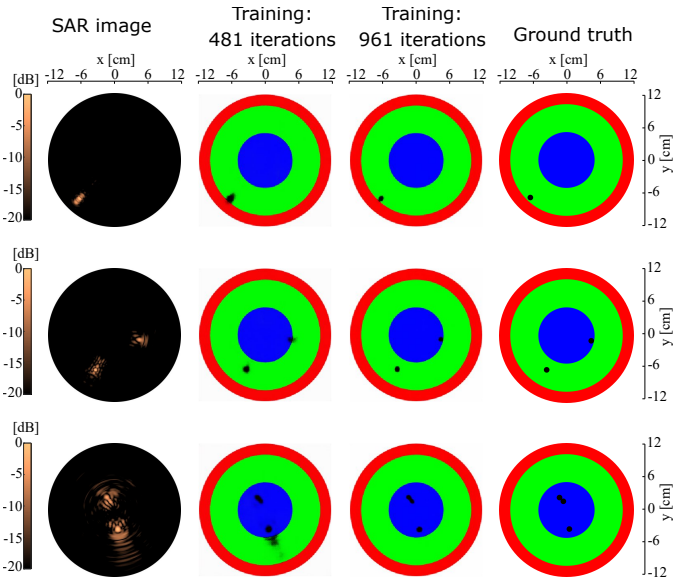

Fig. 5. Output at intermediate stages of the training for several training pairs for the cylindrically-layered media example.

to detect at least two targets with an accurate positioning but it fails to identify all of them. Finally, the last case is similar to the previous one with two very close targets and an additional separated target. In this case, the cGAN provides an intermediate result, enabling the detection of all the targets, including the two close to each other, though one of them is shown slightly smaller.

In order to compare the previous results with conventional approaches to clean the image, the SVD filtering and R-CNN approaches are used [17]. The former one is well-known in subsurface imaging. In this approach, the time domain signals (i.e., after an inverse Fourier transform) are arranged into a matrix. After that, a SVD is performed and the highest singular values are removed, as they are typically due to medium interface reflections. Moreover, the lowest singular values are also set to zero as they are due to noisy reflections. After that, the imaging algorithm is applied [13]. In this research, it was found that filtering the highest singular values did not result in an improvement of the result as they seem to contain relevant information about the targets. Thus, only the lowest singular values have been filtered out. Columns 4 to 6 of Fig. 6b depicts the results using the SVD approach using a gray scale together with an overlay of the different media. In this plot, N_{SVD} refers to the number of maximum singular values which are kept. As it is shown, this technique does not improve the results in this complex problem with high interface interactions as some targets are still significantly blurred, which prevents from identifying close targets and the accurate estimation of their position.

In the case of the R-CNN approach, the same CNN structure as in the faster R-CNN presented in [19] was used except that the input images have two channels. The underlying CNN was trained by using 32x32 pieces of the cGAN training images tagged as target or clutter depending on if they contain one or more targets or not. The total number of training images was 47040. In order to provide a continuous output, rather than a rectangular tagged output, the CNN is moved along 32x32 regions, which are overlapped, so they are classified as target or clutter. If a pixel is estimated as target for several overlapped subimages, then its score is accumulated. The normalized results in the rightmost column of Fig. 6 show that the targets and their positions are correctly identified in most of cases but with a resolution far from the one achieved with cGAN.

Regarding the time increment due to the different approaches, the cGAN postprocessing of the images requires 117.5 ms whereas the SVD preprocessing entails an average time of 5.2 ms. Though the time required to apply the SVD filtering is lower than that required by the cGAN processing, it should be remarked that it is sufficiently low to enable the use of this method in real-time applications. In the case of the R-CNN, the classification of each 32x32 subimage takes 2.8 ms but the application to overlapped subimages increases the total time to 32.12 s.

B. Mm-wave freehand SAR

The freehand problem shown in Fig. 1b is considered in this section. Although freehand scanning can provide very accurate imaging results on real-time, intermediate results with partial acquisition data are expected to be noisy due to the sparse samples. Consequently, the use of cGAN to enhance the partial images is very convenient.

The core of the freehand setup is the FMCW MIMO radar topology exploited in [43]. This topology entails 2 transmitters and 4 receivers sweeping from 57 GHz to 63 GHz. It is important to remark that FMCW radars provide raw data, which differs from the raw data from a stepped-frequency radar like the one supposed in (1). Nevertheless, the imaging technique used in [43] is equivalent to the one described in (3)-(4) as shown in [44].

The entire setup used for the freehand imaging is shown in Fig. 7 and it comprises the aforementioned MIMO radar, whose position is tracked by means of a motion capture system with four infrared cameras and infrared markers attached to

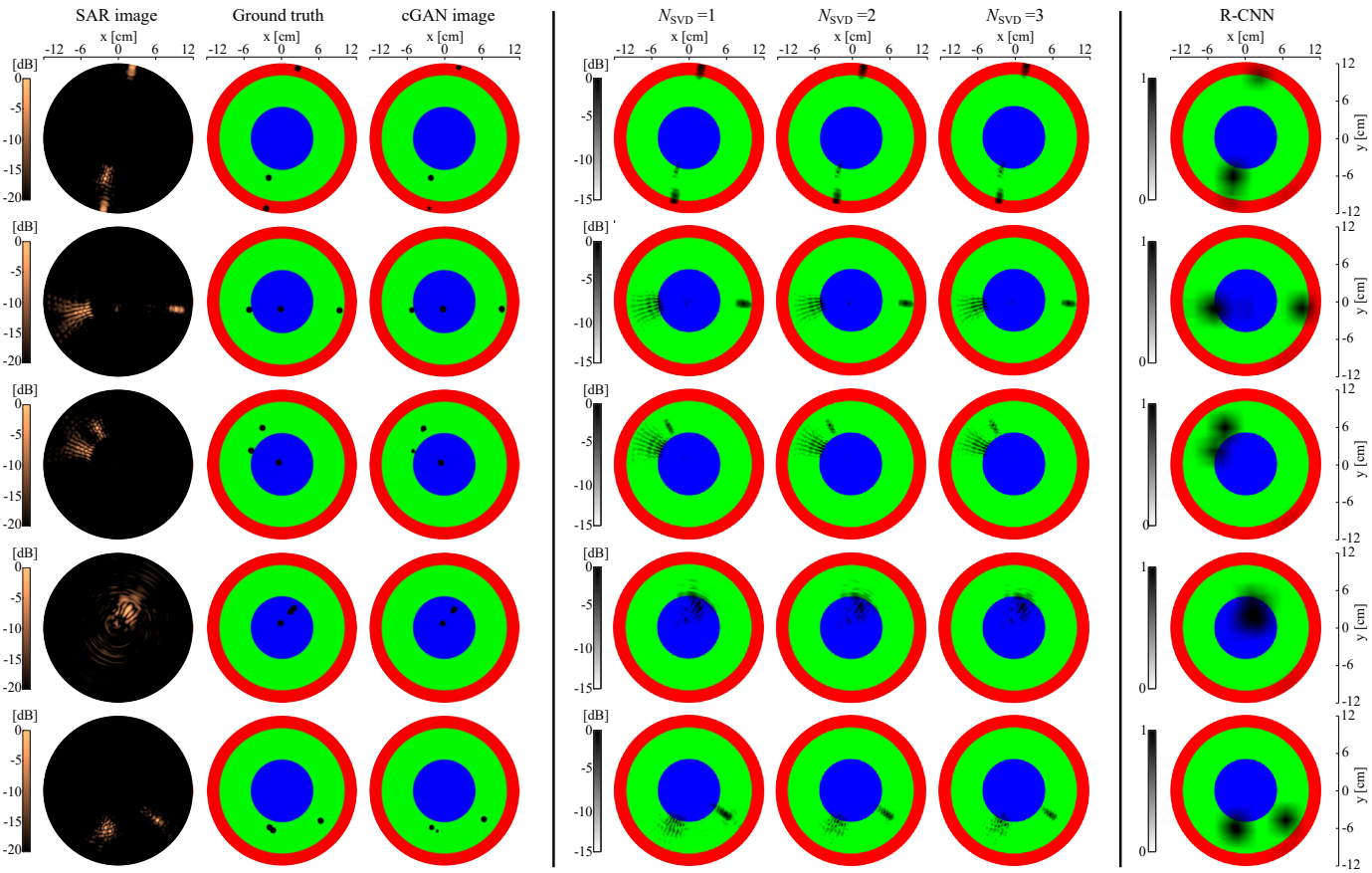

Fig. 6. Imaging of several targets in cylindrically-layered media using the proposed method (third column), SVD filtering (columns 4 to 6), and R-CNN (column 7). The original SAR image and the ground truth are shown in colums 1 and 2, respectively .

the radar case. The radar module is connected by means of a USB cable to a laptop which gathers and processes the pairs of raw FMCW data and the corresponding position.

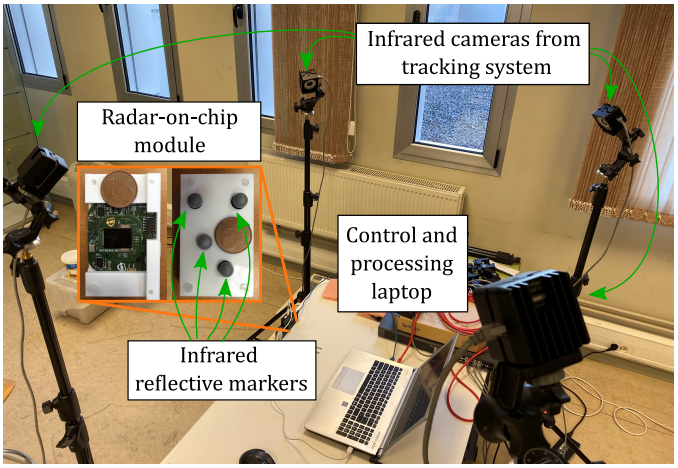

Fig. 7. Setup for the freehand measurements.

In this case, the cGAN is optimized to detect the shape of scissors. For this purpose, the three scissors models shown in Fig. 8 are used. These models were built by tracing public pictures. Each blade was independently traced so that different blade openings can be automatically generated to build a significant dataset. In particular, aperture angles from 0 to 60 degrees were considered. In addition, eight different rotations of the entire scissors were considered together with images flipped along the x- and y-axis. The total number of considered geometries was 800. Although this is a very reduced representation of general scissors models, it is expected to provide a fair distribution so the cGAN can learn to clean the artifacts from the scissors shape.

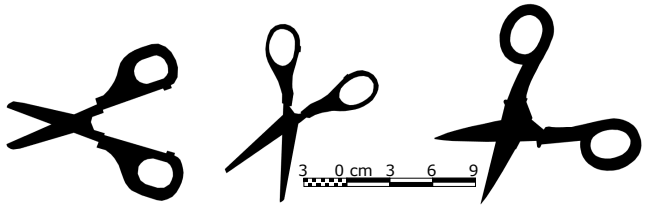

Fig. 8. Three scissors models used during the training. Images are shown for a specific opening and rotation angles.

In order to generate the training dataset, one could consider to artificially introduce artifacts in the image by contaminating the real images without considering the real electromagnetic nature of the problem. Although that approach would be very efficient, as it does not require computationally expensive electromagnetic simulations, it is uncertain if it would properly model the artifacts due to the problems described in section

II. Thus, the flowchart given in Fig. 9, which relies on real electromagnetic modeling, is used. The first step is to pick-up a model from the database of considered geometries. After that, random acquisition positions are calculated. These positions are initially equally spaced on an XY plane of size $20\,\text{cm} \times 20\,\text{cm}$ at a distance of $5\,\text{cm}$ from the target plane. In order to mimic the effect of freehand scanning, the samples are randomly moved by a 3D offset with a standard deviation of $1\,\text{mm}$ for each spatial coordinate. In addition, a random rotation up to 5 degrees is considered for roll, pitch and yaw angles. Next, the acquisition plane is divided into cells of size $2.5\,\text{mm} \times 2.5\,\text{mm}$ so a maximum of two samples per cell is considered in order to avoid oversampled areas. Finally, a 50% of the samples is dropped off to increase the sparseness.

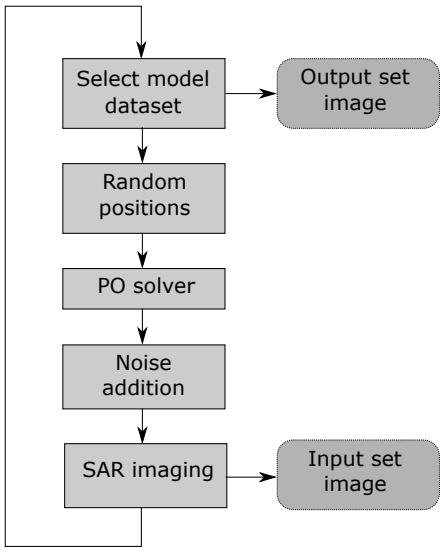

Fig. 9. Scheme for generating the dataset to train the cGAN for the freehand imaging example.

Once the geometry from the dataset and the acquisition positions are available, the problem is simulated using Feko [45] by means of physical optics (PO). Some relevant considerations about this simulation setup are: 1) taking into account the distances, the object is in the near-field of the (synthetic) array, 2) the object points are in the far-field of each separate element so the transmitters can be modeled by means of their far-field pattern even if the application is near-field imaging, 3) the object is electrically large so it is relevant to split it into small pieces (i.e., basis functions) to guarantee that the far-field model of the receiver is also correct.

In order to alleviate the computational burden, the scattered field is only calculated at the central frequency ($60\,\text{GHz}$). Once the scattered data is available, additive Gaussian noise is added so that the signal to noise ratio is set to $20\,\text{dB}$. Next, positioning errors are added to model the tracking errors. The standard deviation of the error for the XY plane and z-axis are $0.5\,\text{mm}$ and $0.2\,\text{mm}$, respectively. In addition, a random error with a standard deviation of 1 degree is also added to the roll, pitch and yaw angles.

Taking into account the noisy scattered field and positioning data, the SAR image is calculated in the target plane. Since the previous errors as well as any calibration error regarding real measurements can have a strong impact in the image phase, only the amplitude of the SAR image is considered for the input dataset. The dynamic range of the SAR images is set to $20\,\text{dB}$.

Fig. 10 depicts the L_1-norm and, analogously to the previous case, as the training converges, the quality of the resulting images is improved with a stable convergence. Some intermediate results are shown in Fig. 11 for different iterations.

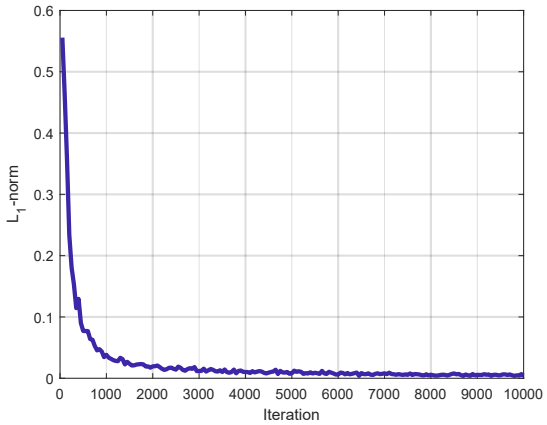

Fig. 10. L_1-norm for the training set for the freehand SAR example.

In order to quantify the quality of the images the target-to-clutter ratio is used:

$$TCR = 10\log\left(\frac{N_c \sum_{(x',y')\in A_t} |\Gamma(x',y')|^2}{N_t \sum_{(x',y')\in A_c} |\Gamma(x',y')|^2}\right), \qquad (8)$$

wherein A_t is the target region, A_c is the clutter region (i.e., the complementary region to A_t), and N_t and N_c are the number of pixels in each region.

Firstly, the system is tested for two simulated models, which were not used in the training. These simulation models as well as the corresponding SAR and cGAN images are shown in Fig. 12. The TCRs for both SAR images are $8.07\,\text{dB}$ and $11.46\,\text{dB}$ (Fig. 12a and Fig. 12d, respectively). Once the images are enhanced by means of the cGAN, the TCRs raise up to $22.5\,\text{dB}$ and $23.48\,\text{dB}$ (Fig. 12b and Fig. 12e, respectively).

In order to further validate the approach, several measurements were conducted. In particular, two scissors models, each in two different positions and openings (see upper row pictures in Fig. 13), were scanned with the prototype presented in [43]. None of these shapes were used during the training, where only synthetic data was considered. The retrieved SAR images and those obtained with the cGAN are depicted in the second and last row of Fig. 13, respectively. As it can be seen, the cGAN is able to remove most of the artifacts in the SAR images at the expense of losing some information in the small details, typically in the handles of the scissors.

For the sake of completeness, the method is compared with two additional methods. First, conventional low-pass filtering techniques are considered. In particular, a median filter with size 3x3 is firstly applied to reduce the speckles. After that, a Gaussian filter with standard deviation of 0.75 is applied and, finally, a threshold in the range of 58-70% is used so pixels

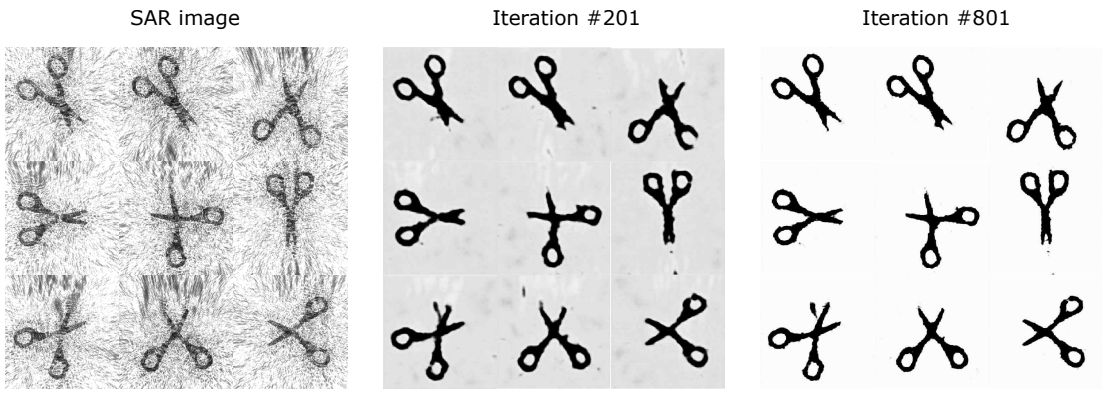

Fig. 11. Output at intermediate stages of the training for several training pairs in the freehand SAR example.

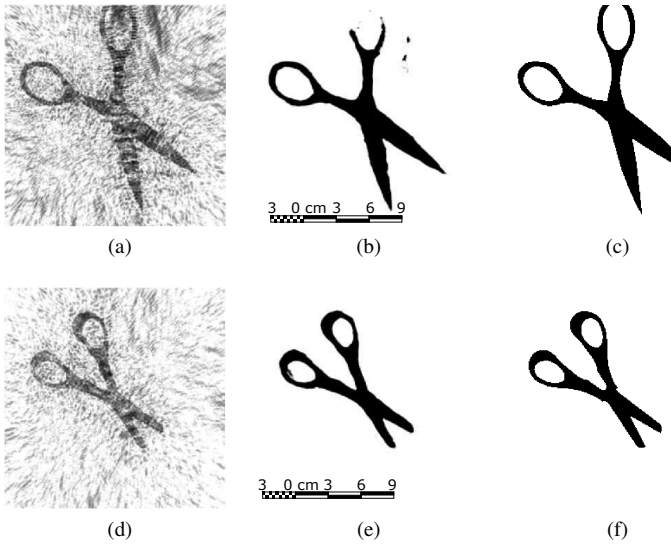

Fig. 12. Results for different simulations of scissors. For the simulation model #1, the images are: (a) the SAR result, (b) the cGAN result and (c) the ground-truth. For the simulation model #2, the images are: (d) the SAR result, (e) the cGAN result and (f) the ground-truth.

are classified as belonging to the target or not. Although this approach contributes to clean the SAR image, in general it is less effective than the cGAN, and it results in shapes much less natural than the ones from the cGAN approach (see row #3 of Fig. 13). Second, the R-CNN is employed by using the same architecture as in the previous example (using only 1 input channel). The training images were generated following the same strategy, resulting in 39200 images. The R-CNN output was roughly following the shape of the target but with a very low resolution. Hence, an extra step was accomplished by using the R-CNN output as a mask for the original result. Although it enables the removal of some of the clutter, it also clips significant regions of the image around the handles (see images of row#4 of Fig. 13).

For the sake of completeness, the results are quantified by means of the TCR in Table II. The cGAN approach clearly outperforms the raw SAR images. Also, after the described low pass filtering is applied, the SAR images are improved but the cGAN provides better results except for model #2, wherein the performance is very close for both techniques. Regarding the R-CNN, as it filters most of the the clutter (but also relevant features such as the handles) the TCR is significantly improved with respect to the the raw SAR images. Nevertheless, the cGAN outperforms R-CNN except for the second model, wherein the TCR is similar with both techniques.

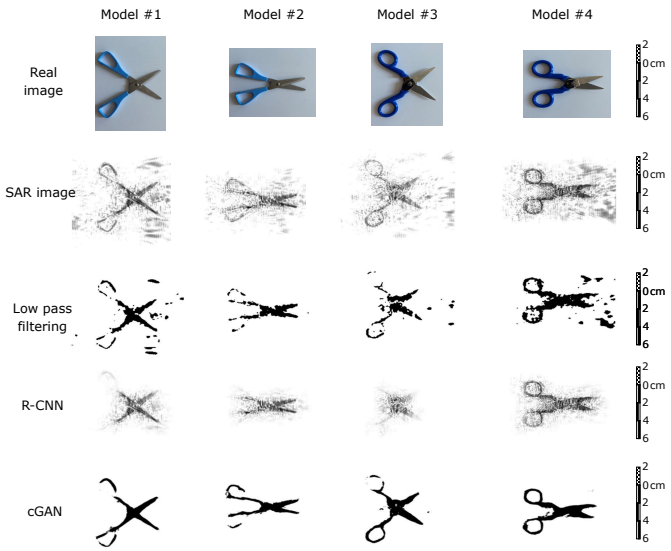

Fig. 13. Results for different measurements of models of scissors using raw SAR results, low pass filtering techniques, R-CNN and cGAN. The corresponding real images are shown on top.

Table II
MEASUREMENT RESULTS COMPARING THE TARGET-TO-CLUTTER RATIO FOR DIFFERENT TARGETS.

Meas. model	#1	#2	#3	#4
SAR	14.97	17.10	14.73	14.55
Low pass filt.	16.50	20.65	18.03	14.89
R-CNN	20.46	20.37	19.55	18.30
cGAN	22.06	20.30	20.22	21.66

Regarding the computational burden, the translation of the images by means of the cGAN and low pass filtering takes

an average time of 107 ms and 108 ms, respectively. Although these times are very dependent on the implementation and supporting hardware (e.g., GPU), it is clear that the cGAN approach does not entail a significant time penalty. In the case of the R-CNN, the subimage and image evaluation takes the same time as in the previous example.

V. Conclusions

Synthetic aperture imaging is a very powerful technique but, if pushed to its limits, it can exhibit some artifacts in the output images. Generative adversarial nets can detect deep features in the image and associate them to clean features learned during the training stage to enhance the quality of these SAR images.

In the case of complex systems, such as those for multilayered media, which suffer from spread and position-dependent point spread function, it has been proved that the cGAN is able to learn the corresponding distribution. Thus, cGANs are suitable to improve the quality of SAR images. The system shows robustness even if multiple responses are combined or if some of them are weak, enabling a clear detection of the targets.

Results have also been studied for the case of freehand approaches, which can suffer from significant artifacts during the intermediate stages due to the sparseness of the sampling and the tracking errors. In this case, good results have been observed for both simulated and measured SAR images in the case of detecting specific targets (scissors). Although the cGAN was able to provide a clean output with minor artifacts, some of the small features (e.g., some parts of the handles) were lost, suggesting that the detection prioritizes large areas. It is also relevant to note that the used cGAN architectures do not incur in a significant time penalty so they are compatible with the real-time performance of the freehand imaging.

Whereas cGANs exhibit clear advantages when dealing with SAR images, they also exhibit some drawbacks. One of the most limiting is that they require a large and representative dataset, which is inherent to machine learning approaches. In this paper, this dataset was generated from electromagnetic simulations reproducing measurement conditions as it is usually not feasible to perform hundreds of measurements to obtain the training pairs (i.e., contaminated and clean image pairs). However, even for this scenario, simulations can become quickly prohibitive due to the computational complexity and, therefore, the generation of training data remains as one of the main challenges. Another drawback that could be found in some problems is that if the number of possible targets becomes very large, the object distribution could become very fuzzy. Consequently, the CNNs would not be effective in detecting and generating features. Thus, it is prudent to avoid abstract or not well-defined problems when dealing with cGANs as the training and detection capabilities could be compromised.

References

[1] L. Tsang, J. A. Kong, and R. T. Shin, *Theory of Microwave Remote Sensing*. New York, NY, USA: Wiley, 1985.

[2] D. M. Sheen, D. L. McMakin, and T. E. Hall, "Three-dimensional millimeter-wave imaging for concealed weapon detection," *IEEE Trans. Microw. Theory Tech.*, vol. 49, no. 9, pp. 1581–1592, September 2001.

[3] S. Ahmed, A. Schiessl, and L. Schmidt, "A novel fully electronic active real-time imager based on a planar multistatic sparse array," *IEEE Trans. Microw. Theory Tech.*, vol. 59, no. 12, pp. 3567–3576, 2011.

[4] S. Kharkovsky and R. Zoughi, "Microwave and millimeter wave nondestructive testing and evaluation - overview and recent advances," *IEEE Instrumentation Measurement Magazine*, vol. 10, no. 2, pp. 26–38, April 2007.

[5] M. T. Ghasr, D. Pommerenke, J. T. Case, A. McClanahan, A. Aflaki-Beni, M. Abou-Khousa, S. Kharkovsky, K. Guinn, F. D. Paulis, and R. Zoughi, "Rapid rotary scanner and portable coherent wideband Q-band transceiver for high-resolution millimeter-wave imaging applications," *IEEE Transactions on Instrumentation and Measurement*, vol. 60, no. 1, pp. 186–197, Jan 2011.

[6] Y. Gao and R. Zoughi, "Millimeter reflectometry as an effective diagnosis tool for skin burn injuries," in *2016 IEEE International Instrumentation and Measurement Technology Conference Proceedings*, 2016, pp. 1–5.

[7] J. M. Lopez-Sanchez and J. Fortuny-Guasch, "3-D radar imaging using range migration techniques," *IEEE Trans. Antennas Propag.*, vol. 48, no. 5, pp. 728–737, May 2000.

[8] Y. Gao, M. T. Ghasr, and R. Zoughi, "Effects of and compensation for translational position error in microwave synthetic aperture radar imaging systems," *IEEE Transactions on Instrumentation and Measurement*, vol. 69, no. 4, pp. 1205–1212, 2020.

[9] X. Tian, Q. Guo, Z. Wang, T. Chang, and H.-L. Cui, "Pragmatic approach to phase self-calibration for planar array millimeter-wave MIMO imaging," *IEEE Transactions on Instrumentation and Measurement*, vol. 70, pp. 1–11, 2021.

[10] M. Fallahpour, J. Case, M. Ghasr, and R. Zoughi, "Piecewise and wiener filter-based SAR techniques for monostatic microwave imaging of layered structures," *IEEE Transactions on Antennas and Propagation*, vol. 62, no. 1, pp. 282–294, Jan 2014.

[11] J. Laviada, B. Wu, M. T. Ghasr, and R. Zoughi, "Nondestructive evaluation of microwave-penetrable pipes by synthetic aperture imaging enhanced by full-wave field propagation model," *IEEE Transactions on Instrumentation and Measurement*, vol. 68, no. 4, pp. 1112–1119, 2019.

[12] B. Wu, Y. Gao, J. Laviada, M. T. Ghasr, and R. Zoughi, "Time-reversal sar imaging for nondestructive testing of circular and cylindrical multi-layered dielectric structures," *IEEE Transactions on Instrumentation and Measurement*, vol. 69, no. 5, pp. 2057–2066, 2020.

[13] M. García-Fernández, Y. Álvarez López, and F. L.-H. Andrés, "Airborne multi-channel ground penetrating radar for improvised explosive devices and landmine detection," *IEEE Access*, vol. 8, pp. 165 927–165 943, 2020.

[14] G. Álvarez-Narciandi, J. Laviada, and F. Las-Heras, "Towards turning smartphones into mmWave scanners," *IEEE Access*, vol. 9, pp. 45 147–45 154, 2021.

[15] G. Álvarez-Narciandi, M. López-Portugués, F. Las-Heras, and J. Laviada, "Freehand, agile, and high-resolution imaging with compact mm-wave radar," *IEEE Access*, vol. 7, pp. 95 516–95 526, 2019.

[16] J. W. Smith and M. Torlak, "Efficient 3-D near-field MIMO-SAR imaging for irregular scanning geometries," *IEEE Access*, vol. 10, pp. 10 283–10 294, 2022.

[17] N. Smitha and V. Singh, "Clutter reduction techniques of ground penetrating radar for detecting subsurface explosive objects," in *2016 International Conference on Information Communication and Embedded Systems (ICICES)*, 2016, pp. 1–8.

[18] V. Kabourek, P. Černý, and M. Mazanek, "Clutter reduction based on principal component analysis technique for hidden objects detection," *Radioengineering*, vol. 21, 04 2012.

[19] L. Zhan, W. You, Q. M. J. Wu, S. Qi, and Y. Ji, "Deep learning-based automatic clutter/interference detection for HFSWR," *Remote Sensing*, vol. 10, no. 10, 2018.

[20] M. Wu, L. Zhang, J. Niu, and Q. M. J. Wu, "Target detection in clutter/interference regions based on deep feature fusion for HFSWR," *IEEE Journal of Selected Topics in Applied Earth Observations and Remote Sensing*, vol. 14, pp. 5581–5595, 2021.

[21] I. Goodfellow, J. Pouget-Abadie, M. Mirza, B. Xu, D. Warde-Farley, S. Ozair, A. Courville, and Y. Bengio, "Generative adversarial nets," in *Advances in Neural Information Processing Systems 27 (NIPS 2014)*, 2014.

[22] J. Guo, B. Lei, C. Ding, and Y. Zhang, "Synthetic aperture radar image synthesis by using generative adversarial nets," *IEEE Geoscience and Remote Sensing Letters*, vol. 14, no. 7, pp. 1111–1115, 2017.

[23] K. Wang, G. Zhang, Y. Leng, and H. Leung, "Synthetic aperture radar image generation with deep generative models," *IEEE Geoscience and Remote Sensing Letters*, vol. 16, no. 6, pp. 912–916, 2019.

[24] Z. Cui, M. Zhang, Z. Cao, and C. Cao, "Image data augmentation for SAR sensor via generative adversarial nets," *IEEE Access*, vol. 7, pp. 42 255–42 268, 2019.
[25] H. Huang, F. Zhang, Y. Zhou, Q. Yin, and W. Hu, "High Resolution SAR Image Synthesis with Hierarchical Generative Adversarial Networks," in *IGARSS 2019 - 2019 IEEE International Geoscience and Remote Sensing Symposium*, 2019, pp. 2782–2785.
[26] P. Wang and V. M. Patel, "Generating high quality visible images from SAR images using CNNs," in *2018 IEEE Radar Conference (RadarConf18)*, 2018, pp. 0570–0575.
[27] J. Ai, G. Fan, Y. Mao, J. Jin, M. Xing, and H. Yan, "An improved SRGAN based ambiguity suppression algorithm for SAR ship target contrast enhancement," *IEEE Geoscience and Remote Sensing Letters*, vol. early access, pp. 1–5, 2021.
[28] J. Guan, S. Madani, S. Jog, S. Gupta, and H. Hassanieh, "Through fog high-resolution imaging using millimeter wave radar," in *2020 IEEE/CVF Conference on Computer Vision and Pattern Recognition (CVPR)*, 2020, pp. 11 461–11 470.
[29] X. Mou, X. Chen, J. Guan, Y. Dong, and N. Liu, "Sea clutter suppression for radar PPI images based on SCS-GAN," *IEEE Geoscience and Remote Sensing Letters*, vol. 18, no. 11, pp. 1886–1890, 2021.
[30] W. Jiang, Y. Ren, Y. Liu, and J. Leng, "Artificial neural networks and deep learning techniques applied to radar target detection: A review," *Electronics*, vol. 11, no. 1, 2022. [Online]. Available: https://www.mdpi.com/2079-9292/11/1/156
[31] X. Tang, D. Li, W. Cheng, J. Su, and J. Wan, "A novel sea clutter suppression method based on deep learning with exploiting time-frequency features," in *2021 IEEE 5th Advanced Information Technology, Electronic and Automation Control Conference (IAEAC)*, vol. 5, 2021, pp. 2548–2552.
[32] J. Laviada, G. Álvarez Narciandi, and F. Las-Heras, "Synthetic aperture radar images for cGAN training," 2022. [Online]. Available: https://dx.doi.org/10.21227/5gzt-cm67
[33] C. Liu, M. T. A. Qaseer, and R. Zoughi, "Influence of antenna pattern on synthetic aperture radar resolution for NDE applications," *IEEE Transactions on Instrumentation and Measurement*, vol. 70, pp. 1–11, 2021.
[34] X. Tian, T. Chang, and H.-L. Cui, "Short-range millimeter-wave imaging in the presence of array element position deviation," *IEEE Transactions on Microwave Theory and Techniques*, in press.
[35] J. Laviada, B. Wu, M. T. Ghasr, and R. Zoughi, "Nondestructive evaluation of microwave-penetrable pipes by synthetic aperture imaging enhanced by full-wave field propagation model," *IEEE Transactions on Instrumentation and Measurement*, vol. 68, no. 4, pp. 1112–1119, April 2019.
[36] T. Karras, S. Laine, and T. Aila, "A style-based generator architecture for generative adversarial networks," *CoRR*, vol. abs/1812.04948, 2018. [Online]. Available: http://arxiv.org/abs/1812.04948
[37] P. Isola, J.-Y. Zhu, T. Zhou, and A. A. Efros, "Image-to-image translation with conditional adversarial networks," 2018, [Online]. Available: arXiv:1611.07004.
[38] N. Hayatbini, B. Kong, K. lin Hsu, P. Nguyen, S. Sorooshian, G. Stephens, C. Fowlkes, R. Nemani, and S. Ganguly, "Conditional generative adversarial networks (cGANs) for near real-time precipitation estimation from multispectral GOES-16 Satellite Imageries—PERSIANN-cGAN," *Remote Sensing*, vol. 11, no. 19, 2019. [Online]. Available: https://www.mdpi.com/2072-4292/11/19/2193
[39] H. Zhang, V. Sindagi, and V. M. Patel, "Image de-raining using a conditional generative adversarial network," *CoRR*, vol. abs/1701.05957, 2017. [Online]. Available: http://arxiv.org/abs/1701.05957
[40] J. Zhang, M. Guo, and J. Fan, "A novel generative adversarial net for calligraphic tablet images denoising," *Multimed Tools Appl*, vol. 79, no. 17, p. 119–140, 2020.
[41] K. Schawinski, C. Zhang, H. Zhang, L. Fowler, and G. K. Santhanam, "Generative adversarial networks recover features in astrophysical images of galaxies beyond the deconvolution limit," *Monthly Notices of the Royal Astronomical Society: Letters*, p. slx008, Jan 2017. [Online]. Available: http://dx.doi.org/10.1093/mnrasl/slx008
[42] J. Pinkney, "Matlab implementation of pix2pix," 2021, [Online]. Available: https://github.com/matlab-deep-learning/pix2pix.
[43] G. Álvarez-Narciandi, J. Laviada, and F. Las-Heras, "Freehand mm-wave imaging with a compact MIMO radar," *IEEE Transactions on Antennas and Propagation*, vol. 69, no. 2, pp. 1224–1229, 2021.
[44] R. K. Amineh, "Developments in three-dimensional near-field imaging with FMCW radar: A comparative study," *AIMS Electronics and Electrical Engineering*, vol. 4, no. 4, pp. 359–368, 2020.
[45] *FEKO User Manual, Suite 6.2*. Stellenbosch, South Africa: EM Softw. Syst. S.A. (Pty) Ltd., 2013.

Jaime Laviada was born in Gijón, Spain. He received the M.S. degree in telecommunication engineering and the Ph.D. degree from the Universidad de Oviedo, Spain, in 2005 and 2010, respectively. In 2006, he joined the research group Signal Theory and Communications, Universidad de Oviedo, where he has been involved in multiple national and European projects as well as contracts with several companies. In 2015, he moved to the Antennas Group of the Universidad Pública de Navarra with a National Postdoctoral Fellowship collaborating in several applied research projects. Finally, he moved back to the Universidad de Oviedo, where he currently holds a position of Associate Professor. In addition, he has been a Visiting Scholar with the Electromagnetics and Communications Laboratory, Pennsylvania State University, from 2007 to 2008, and with the Applied Microwave NonDestructive Testing Laboratory, Missouri S&T, in 2017. His research interests include numerical techniques applied to EM imaging, antenna measurements, method of moments, and antenna pattern synthesis.

Guillermo Álvarez-Narciandi received the M.Sc. degree in telecommunication engineering and the Ph.D. degree from the University of Oviedo, Gijón, Spain, in 2016 and 2020, respectively. He was a visiting student with Stanford University, Stanford, CA, USA, in 2014; a Visiting Scholar with the University of Pisa, Italy, in 2018; and with the Institute of Electronics, Microelectronics and Nanotechnology, University of Lille, France, in 2019. In 2022, he joined Queen's University Belfast, as a Research Fellow with the Centre for Wireless Innovation. He received the AMTA 2019 Student Paper Award (Second Place) and the Special Award to the Best Entrepreneurship Initiative in XV Arquímedes National Contest, in 2017, for the development of a RFID-based location system. His research interests include radar systems and imaging techniques, antenna diagnosis and characterization systems, localization and attitude estimation systems, and RFID technology.

Fernando Las-Heras (Senior Member, IEEE) received the M.S. and Ph.D. degrees in telecommunication engineering from the Technical University of Madrid (UPM), in 1987 and 1990, respectively. From 1988 to 1990, he was a National Graduate Research Fellow, and from 1991 to 2000, he held a position of Associate Professor with the Department of Signal, Systems and Radio Communications, UPM. Since 2003, he has been held a Full-Professor position with the University of Oviedo, where he was the Vice-Dean for Telecommunication Engineering with the Technical School of Engineering, Gijón, in 2004 to 2008. Since 2001, he has been heading the research group Signal Theory and Communications TSC-UNIOVI with the Department of Electrical Engineering, University of Oviedo. He was a Visiting Lecturer with the National University of Engineering, Peru, in 1996, a Visiting Researcher with Syracuse University, New York, in 2000, and a short-term Visiting Lecturer with ESIGELEC, France, from 2005 to 2011. From 2005 to 2015, he held the Telefónica Chair on "RF Technologies," "ICTs applied to Environment," and "ICTs and Smart cities" with the University of Oviedo. He was a member of the board of directors of the IEEE Spain Section, from 2012 to 2015, member of the board IEEE Microwaves and Antennas Propagation Chapter (AP03/MTT17), from 2016 to 2017, member of the Science, Technology and Innovation Council, Asturias, from 2010 to 2012, and President of the Professional Association of Telecommunication Engineers, Asturias. He has authored scientific articles in the areas of antennas, EM scattering, metamaterials and inverse problems with application to antenna measurement (NF-FF, diagnostics and holography), electromagnetic imaging (security and NDT) and localization, developing computational electromagnetics algorithms and technology on microwaves, millimeter wave, and THz frequency bands.